

This work is on a Creative Commons Attribution 4.0 International (CC BY 4.0) license, <https://creativecommons.org/licenses/by/4.0/>. Access to this work was provided by the University of Maryland, Baltimore County (UMBC) ScholarWorks@UMBC digital repository on the Maryland Shared Open Access (MD-SOAR) platform.

Please provide feedback

Please support the ScholarWorks@UMBC repository by emailing scholarworks-group@umbc.edu and telling us what having access to this work means to you and why it's important to you. Thank you.



Research article

Navid Rajil, Alexei Sokolov, Zhenhuan Yi, Garry Adams, Girish Agarwal, Vsevolod Belousov, Robert Brick, Kimberly Chapin, Jeffrey Cirillo, Volker Deckert, Sahar Delfan, Shahriar Esmaeili, Alma Fernández-González, Edward Fry, Zehua Han, Philip Hemmer, George Kattawar, Moochan Kim, Ming-Che Lee, Chao-Yang Lu, Jon Mogford, Benjamin Neuman, Jian-Wei Pan, Tao Peng, Vincent Poor, Steven Scully, Yanhua Shih, Szymon Suckewer, Anatoly Svidzinsky, Aart Verhoef, Dawei Wang, Kai Wang, Lan Yang, Aleksei Zheltikov, Shiyao Zhu, Suhail Zubairy and Marlan Scully*

A fiber optic–nanophotonic approach to the detection of antibodies and viral particles of COVID-19

<https://doi.org/10.1515/nanoph-2020-0357>

Received July 1, 2020; accepted August 31, 2020; published online September 29, 2020

Abstract: Dr. Deborah Birx, the White House Coronavirus Task Force coordinator, told NBC News on “Meet the Press” that “[T]he U.S. needs a ‘breakthrough’ in coronavirus testing to help screen Americans and get a more accurate picture of the virus’ spread.” We have been involved with biopathogen detection since the 2001 anthrax attacks and were the first

to detect anthrax in real-time. A variation on the laser spectroscopic techniques we developed for the rapid detection of anthrax can be applied to detect the Severe Acute Respiratory Syndrome-Corona Virus-2 (SARS-CoV-2 virus). In addition to detecting a single virus, this technique allows us to read its surface protein structure. In particular, we have been conducting research based on a variety of quantum optical approaches aimed at improving our ability to detect Corona Virus Disease-2019 (COVID-19) viral infection.

The list of coauthors represents only a fraction of the team working on the real-time detection of pathogens from anthrax to SARS-CoV-2.

They are the team members most involved in the current COVID-19 research and we thank coeditors Federico Capasso and Dennis Couwenberg for the invitation to contribute to this volume honoring the COVID-19 workers.

Navid Rajil, Alexei Sokolov and Zhenhuan Yi: contributed equally to this work.

***Corresponding author: Marlan Scully**, Texas A&M University, College Station, TX 77843, USA; Baylor University, Waco, TX 76798, USA; and Princeton University, Princeton, NJ 08544, USA, E-mail: scully@tamu.edu

Navid Rajil, Alexei Sokolov, Zhenhuan Yi, Garry Adams, Girish Agarwal, Robert Brick, Kimberly Chapin, Jeffrey Cirillo, Sahar Delfan, Shahriar Esmaeili, Alma Fernández-González, Edward Fry, Zehua Han, George Kattawar, Moochan Kim, Ming-Che Lee, Tao Peng, Anatoly Svidzinsky, Aart Verhoef, Kai Wang and Suhail Zubairy, Texas A&M University, College Station, TX 77843, USA. <https://orcid.org/0000-0002-9220-4080> (M. Kim)

Vsevolod Belousov, Shemyakin–Ovchinnikov Institute of Bioorganic Chemistry, Russian Academy of Sciences, Moscow 117997, Russia; Pirogov Russian National Research Medical University, Moscow 117997, Russia; and Federal Center of Brain Research and

Neurotechnologies of the Federal Medical Biological Agency, Moscow 117997, Russia

Volker Deckert, Texas A&M University, College Station, TX 77843, USA; Leibniz Institute of Photonic Technology, 07745 Jena, Germany; and Friedrich Schiller University, 07743 Jena, Germany

Philip Hemmer, Texas A&M University, College Station, TX 77843, USA; and Zavoisky Physical-Technical Institute, 420029 Kazan, Russia
Chao-Yang Lu and Jian-Wei Pan, University of Science and Technology of China, Hefei, Anhui, 230026, P. R. China

Jon Mogford, Texas A&M University System, College Station, TX 77840, USA

Benjamin Neuman, Texas A&M University, College Station, TX 77843, USA; and Texas A&M University, Texarkana, TX 75503, USA

Vincent Poor, Princeton University, Princeton, NJ 08544, USA

Steven Scully, Collins Aerospace, Richardson, TX 75082, USA

Yanhua Shih, University of Maryland, Baltimore County, 1000 Hilltop Circle, Baltimore, MD 21250, USA

Szymon Suckewer, Texas A&M University, College Station, TX 77843, USA; and Princeton University, Princeton, NJ 08544, USA

Dawei Wang and Shiyao Zhu, Zhejiang University, 38 Zheda Rd, Hangzhou, 310027, P. R. China

Lan Yang, Washington University, St. Louis, MO 63130, USA

Aleksei Zheltikov, Texas A&M University, College Station, TX 77843, USA; International Laser Center, Moscow State University, Moscow 119992, Russia; and Russian Quantum Center, Skolkovo, Moscow Region, 143025, Russia

Indeed, the detection of a small concentration of antibodies, after an infection has passed, is a challenging problem. Likewise, the early detection of disease, even before a detectible antibody population has been established, is very important. Our team is researching both aspects of this problem. The paper is written to stimulate the interest of both physical and biological scientists in this important problem. It is thus written as a combination of tutorial (review) and future work (preview). We join Prof. Federico Capasso and Editor Dennis Couwenberg in expressing our appreciation to all those working so heroically on all aspects of the COVID-19 problem. And we thank Drs. Capasso and Couwenberg for their invitation to write this paper.

Keywords: detection of SAR-CoV-2 virus; hollow-core fibers; laser spectroscopic technique; nanophotonics.

1 Introduction

As the anthrax attacks and the present pandemic demonstrate, improved strategies to detect viral [1] and bacterial pathogens [2] are urgently needed. Recognizing the importance of the problem, our team has been researching a variety of quantum optical techniques aimed at improving the detection of the Corona Virus Disease-2019 (COVID-19) viral infection.

Much, but not all, of our present work follows on our earlier research using the laser spectroscopic technique called Coherent anti-Stokes Raman scattering (CARS). In particular, here, we utilize innovative fiber optic platforms for antibody and virus detection based on a multichannel fiber sensor such as that sketched in Figure 2a–c.

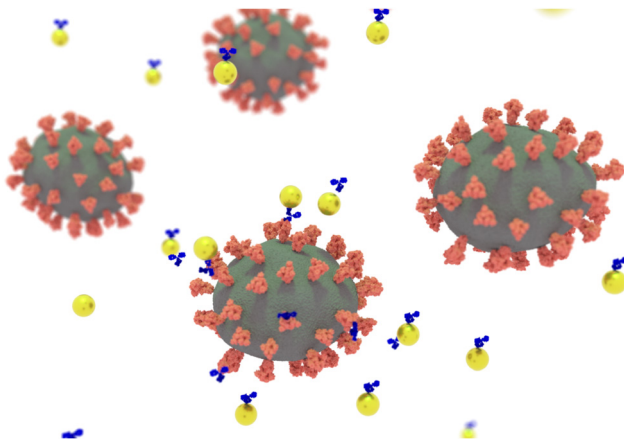


Figure 1: The virion (green) with red spikes, gold nanoparticles (gold) and the antibodies against Severe Acute Respiratory Syndrome-Corona Virus-2 (SARS-CoV-2) (blue). The virion is approximately 100 nm in diameter, the gold nanoparticles are about 40 nm in diameter, and the antibodies are about 10 nm in diameter, respectively.

The present paper focuses on new approaches, building on existing work in modern optics and biochemistry, and is (hopefully) written in a tutorial fashion in hopes of drawing a broader participation from both physical and biological scientists to this important problem.

Figure 1 shows an illustration of virion attachment to antibodies produced by host immune systems. In the present paper, we: (1) develop a coherent laser technique, tailored to the detection of antibodies in the blood and (2) engineer a new approach to detect the presence of Severe Acute Respiratory Syndrome-Corona Virus-2 (SARS-CoV-2 virus), the causative agent of COVID-19, via a fiber-based reverse-transcription polymerase chain reaction (RT-PCR) test.

Central to the broad functionality of the present approach is an optical platform such as shown in Figure 2a–c. In general, we intend to combine microfluidic, optical-interrogation, and PCR-/RT-PCR–amplified nucleic acid identification capabilities. An analyte, such as a blood sample, can flow through the air holes that run along the fiber length [3] and thus form a periodic (Figure 2b) or a spatially chirped (Figure 2c) photonic lattice within a cylindrical rod of host glass. The geometry of this lattice along with its pitch, the diameter of air holes (from 1 to 50 μm [4]), and the glass-analyte index step define the structure of field modes supported by the fiber [5, 6]. When coupled into one of its guided modes, an optical field tends to peak within high-index glass channels (with a notable exception of hollow-core photonic crystal fibers. Its evanescent tails, however, can interact with the analyte (Figure 2a), driving its optical response through a linear [3] or nonlinear [7, 8] optical process, thus providing an optical readout for the detection of viruses and other microorganisms in the analyte. With suitable optimization of the fiber structure, the optical readout can be dramatically enhanced due to improved spatial overlap between the optical field and the analyte (Figure 2a), improving, sometimes by several orders of magnitudes, the sensitivity of antibody and/or nucleic acid identification and, hence as is discussed below, coronavirus detection.

2 Biophotonic SARS-CoV-2 detection schemes

2.1 Fiber-optical antibody tests

It is our intention that the present approach will result in an improved antibody test, with increased sensitivity and reduced false counts. We envision that, due to the improved characteristics at a relatively low production

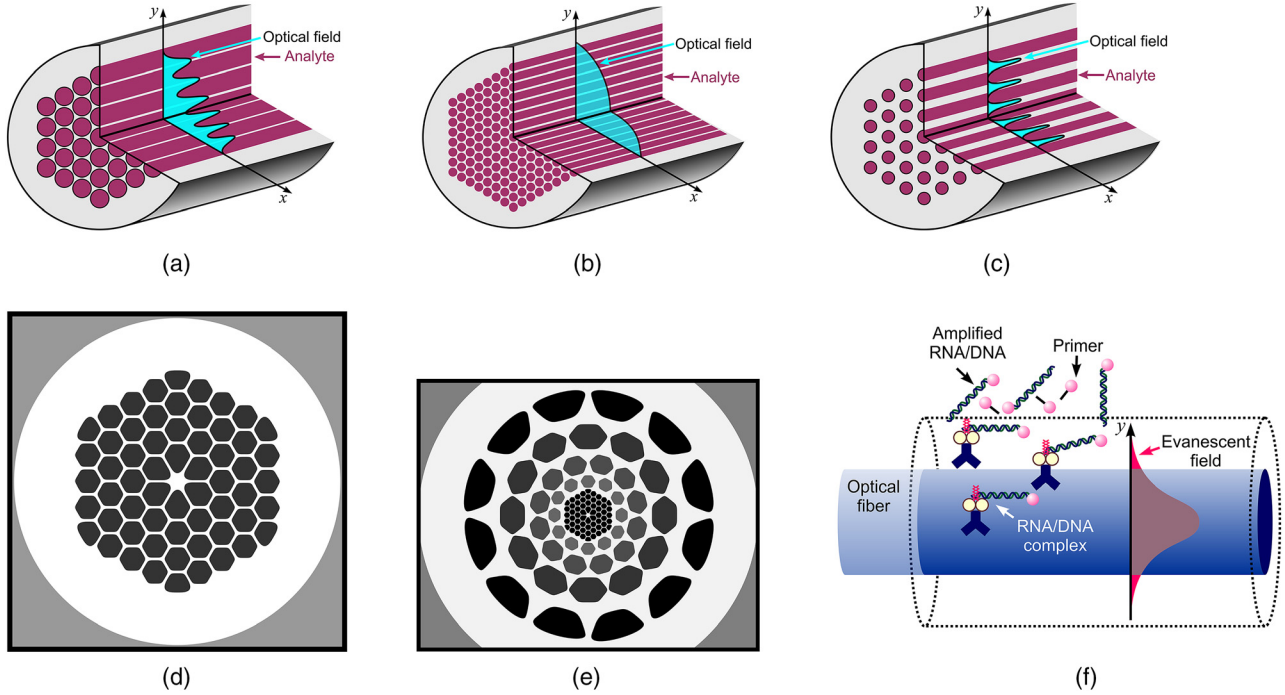


Figure 2: Schematics of the multichannel fiber sensor (a–c) and optical fiber structures (d, e) designed for the sensor. Shown in (f) is a fiber optic fluorometric sensor for the detection of polymerase chain reaction (PCR)–amplified DNA [26].

cost, these tests will become available to a broad population, not limited only to suspected COVID-19 cases. In pursuing this, we build upon the existing ideas, based on the human IgG and IgM antibody property to bind to SARS-CoV-2–specific proteins, and on the availability of antigens capable of binding the IgG and IgM antibodies. We extend prior work by using fluorescent markers together with quantum optical techniques such as higher order, e.g., Brown-Twiss, correlations, etc. In general, we employ optical detection configurations that will make sensitive quantitative measurements with relatively low levels of antibodies. The proposed “fiber” optical scheme is sketched below in Figure 3.

In particular, we shall illustrate our approach by concentrating on IgM and IgG antibodies against SARS-CoV-2 in blood as in Figure 3. There, we see blood mixed with buffer solution containing fluorescent nanoparticles (FNPs) such as nitrogen vacancy nanodiamonds, upconversion nanoparticles or semiconductor quantum dots (QDs), which have been coated with an antigen protein designed from the surface spike protein of SARS-CoV-2. In other words, the QDs, thus coated, look like a SARS-CoV-2 virus to the antibodies and are conjugated (bound) to the antibody as in Figure 3a.

The next step involves forcing the antibody-QD fluid through the tube or fiber optics waveguide, where it binds with the secondary antibodies (anti-antibody) that are

themselves “stuck” to the (properly coated, Section 3) walls. The QDs are now fixed in place and, when driven by an external laser as in Figure 3, can constitute a lasing configuration. Thus, when mirrors are included, the system will “lase” when the antibody particle number (and therefore the antibody count) increases beyond a certain number.

The present scheme provides another way to gather and utilize data. For example, the steady-state photon statistical distribution is given by

$$P(n) = \left(\frac{\mathcal{A}}{\mathcal{B}}\right)! \left(\frac{\mathcal{A}^2}{\mathcal{B}\mathcal{E}}\right)^n \frac{1}{(n + \frac{\mathcal{A}}{\mathcal{B}})} \frac{1}{F(1; \frac{\mathcal{A}}{\mathcal{B}} + 1; \frac{\mathcal{A}^2}{\mathcal{B}\mathcal{E}})}, \quad (1)$$

where F is the confluent hypergeometric function, $\mathcal{A} = 2r\left(\frac{\xi}{\gamma}\right)^2$ is the gain that is directly proportional to the antibody count and \mathcal{E} is governed by the cavity quality factor, and $\mathcal{B} = \frac{4g^2}{\gamma^2}\mathcal{A}$ where g is the atom-field coupling and γ is the radiative decay rate (11.2 of Ref. [9]).

From Eq. (1), the average number of photons in the cavity is given by

$$\langle n \rangle \cong \frac{\mathcal{A}}{\mathcal{E}} \left(\frac{\mathcal{A} - \mathcal{E}}{\mathcal{B}} \right), \quad (2a)$$

and the variance is found from

$$\langle n^2 \rangle - \langle n \rangle^2 = \frac{\mathcal{A}^2}{\mathcal{B}\mathcal{E}}. \quad (2b)$$

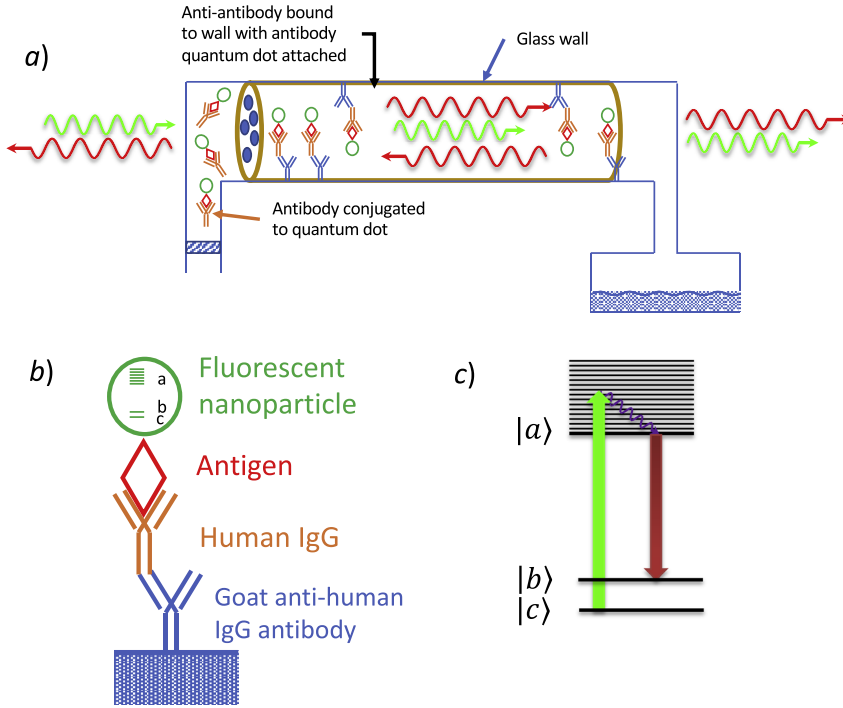


Figure 3: (a) Depicts anti-antibody + antibody-quantum pairs stuck to wall, with the bound pair configuration shown in (b) and the Raman level structure shown in (c).

The fiber bundle configuration can be capped with Bragg reflectors which have a high reflectivity resulting in a cavity loss rate of $\mathcal{E} = (c/l)(1 - R)$, where R is the reflection coefficient. For a “high Q ” configuration with $l \approx 1$ cm the loss rate $\mathcal{E} \equiv \nu/Q \approx 10^6 - 10^7$ s $^{-1}$, where ν is the frequency of light. Using the fact that the coupling constant $g = \frac{\varphi}{\hbar} \sqrt{\frac{\hbar\nu}{\epsilon_0 V}}$, where $V = \pi d^2 l$ and radiative spontaneous decay rate $\gamma_r = \varphi^2 \nu^3 / 3\pi\hbar\epsilon_0 c^3$, we may write \mathcal{A} as

$$\mathcal{A} = 2r \left(\frac{g}{\gamma_t} \right)^2 = \left\{ \frac{3}{2\pi^2} \right\} \frac{c}{l} N \frac{\lambda^2}{d^2} \frac{\gamma_r}{\gamma_t}, \quad (3)$$

with antibody number N , wavelength of photons λ , fiber hole radius d , and effective decay rate γ_t . At threshold where $\mathcal{A} = \mathcal{E}$, we find the antibody number

$$N = \left(\frac{2\pi^2}{3} \right) \frac{d^2}{\lambda^2} \frac{\gamma_t}{\gamma_r} (1 - R). \quad (4)$$

On the other hand, if we have no mirrors then the photon flux at $z = l$ will be given by

$$\frac{d\langle n \rangle}{dz} = \frac{1}{c} \mathcal{A} \langle n \rangle = \left(\frac{3}{2\pi^2} \right) \frac{N}{l} \frac{\lambda^2}{d^2} \frac{\gamma_r}{\gamma_t} \langle n \rangle$$

so that

$$\langle n(l) \rangle = \left(\exp \frac{\mathcal{A} l}{c} \right) \langle n(0) \rangle \approx 1 + \left(\frac{3}{2\pi^2} \right) N \frac{\lambda^2}{d^2} \frac{\gamma_r}{\gamma_t}. \quad (5)$$

So to detect one photon beyond the incident photon number of $\langle n(0) \rangle = 1$, we have the necessary antibody number

$$N = \left(\frac{2\pi^2}{3} \right) \frac{d^2}{\lambda^2} \frac{\gamma_t}{\gamma_r}. \quad (6)$$

The effect of adding “mirror” shows that (4) is smaller than (6) by the factor $(1 - R)$. That is to say the treated fiber bundle is more sensitive when the Bragg mirrors are in phase.

2.2 Using a cavity Quantum Electrodynamics (QED) platform for enhancing detection for antibodies via fluorescence

Biomarkers like green fluorescent proteins are extensively used for detecting tagged biomolecules and antibodies. Here, we suggest a new platform, where fluorescence detection can be enhanced especially for situations where either the fluorescent yield is low or the density of biomolecules is low. We make use of the well-known Purcell effect from the field of cavity QED, a field that was honored by the award of the Nobel Prize to S. Haroche. The new platform is sketched in Figure 4, with the test sample in a capillary or hollow-core fiber as indicated in the figure, i.e., antigen with human IgG (Figure 3b). Antibodies tagged to biomarkers are detected by fluorescence, which is enhanced as the system is contained inside a high quality cavity. Enhancement in fluorescence could be many times that in the absence of the cavity [10]. The

result depends on the quality factor Q of the cavity. The number of photons per second detected outside the cavity is $\left(\frac{2g^2}{\kappa}\right)$ times the number of excitations inside the cavity and hence, in technical terms, the enhancement factor is $\frac{3\lambda^3 Q}{4\pi^2 V}$, where V is the volume of the cavity and λ is the wavelength of transition. In other words, fluorescence probability in the direction of the cavity axis (thin red arrow labeled as detection Figure 4) is given by the factor $\left(\frac{3\lambda^3 Q}{4\pi^2 V}\right)\gamma_r$. For N active molecules in the cavity the net fluorescence photon flux I along the cavity axis will be

$$I = \left(\frac{3\lambda^3 Q N}{4\pi^2 V} \right) \gamma_r \quad (7)$$

and thus

$$N = \frac{4\pi^2 V}{3\lambda^3 \gamma_r Q} I. \quad (8)$$

Note that the quality factor, Q , of the cavity is inversely proportional to the cavity leakage, which is proportional to $(1-R)$, where R is the reflection coefficient of the mirror. It is therefore counter intuitive (but true) that the signal is enhanced. The enhancement of the detected signal originates from the Purcell effect. The measurement of the fluorescence using the scheme of Figure 4 can be highly beneficial for the detection of a small number of IgG molecules attached to antigen-conjugated FNP. In addition, we can improve the detection of IgG by reducing the volume of the cavity and, thus, micron size cavities would be recommended.

Spherical dielectric microresonators supporting whispering gallery modes (WGMs) (see Figure 5) could be an important variation of the above platform. WGMs are resonances of a wave field that are confined inside a cavity with smooth edges. They correspond to standing waves in the cavity. Electromagnetic WGMs with ultra-high Q factors, low mode volumes, and small resonators supporting

them are the objective (see Appendix B). For example, a quality factor of $Q = 8 \times 10^9$ has been measured at $\lambda = 633$ nm in fused silica [11, 12] and $Q = 3 \times 10^{11}$ at $\lambda = 1.5$ μm for crystalline CaF_2 [13].

Since the evanescent field of WGMs protrudes outside the resonator volume, such modes are affected by the environment in which the resonator is placed. The environment shifts the resonant frequencies. Because whispering gallery resonators can have extremely large Q -factors (small linewidth) a shift in their resonant frequencies is easily measured. This means that they act as very sensitive sensors which can be affected by chemical (or bio) composition of their surroundings.

Figure 5 shows a possible scheme for measuring the presence of viruses or antibodies (with single particle resolution [14]) that bind to the surface of a glass microsphere. Coupling is achieved by a tapered optical fiber, and a tunable near Infrared laser that sweeps across different wavelengths to determine the resonance frequencies of the resonator (on-resonance transmission of the laser beam through the optical fiber drops), which directly depend on the number of bound antibodies.

The use of light transmission is a very sensitive tool for the detection of antibodies and can work even without the use of labels [15–20]. This technique has the capability of detecting a single nanoparticle of about 20 nm as demonstrated by Lan Yang et al. [15, 21]. The transmitted spectra could be considerably shifted due to the interaction with the WGM's. The shifts will be proportional to the number of active molecules on the surface of microresonator.

2.3 Photonic PCR for SARS-CoV-2 detection

In this subsection, we propose a photonic platform for real-time polymerase chain reaction (qPCR) and reverse-

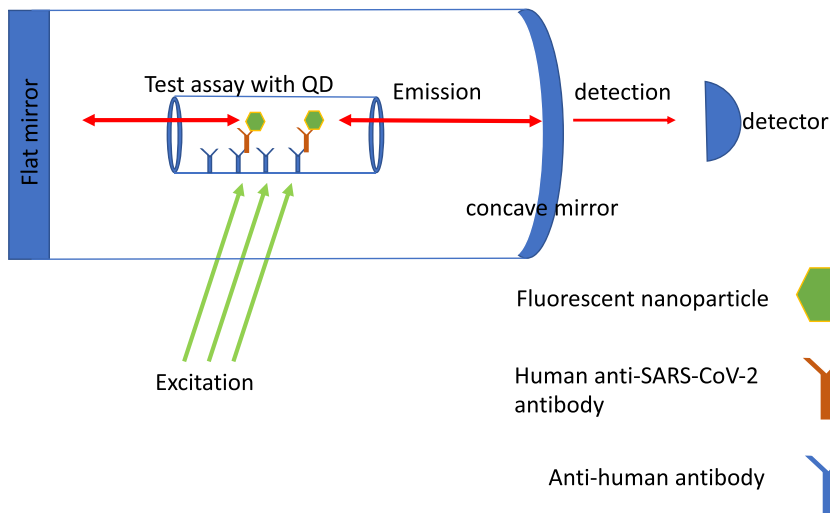


Figure 4: Excitation in one-sided cavity. The green arrows show the excitation light. The red double-arrows show the fluorescence from quantum dots inside the capillary tube. The red arrow on the right shows the output of the cavity which is collected by the detector. Details of the test capillary inside the cavity are shown in Figure 3.

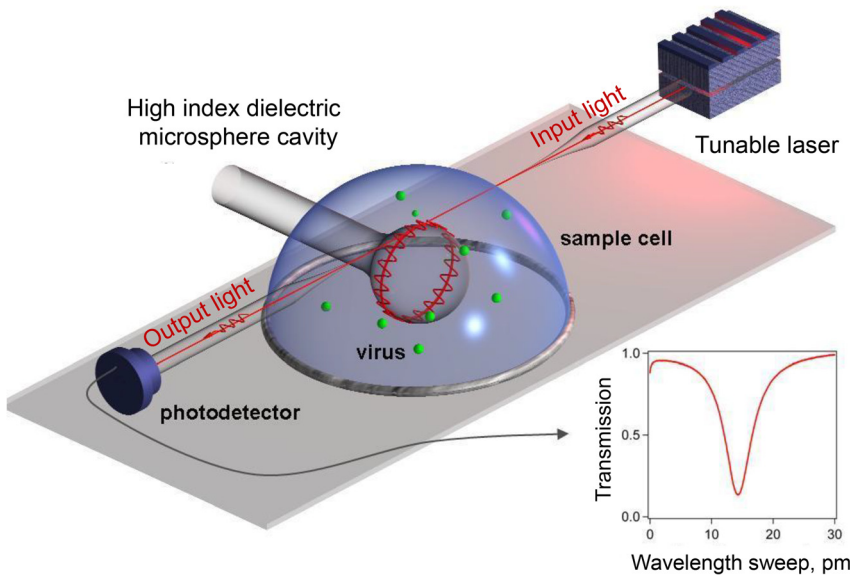


Figure 5: Measuring the presence of a virus using a whispering gallery resonator. As virus molecules bind to the surface, the resonant wavelength position shifts, which is measured by the photodetector. Adapted from F. Vollmer et al. “Single virus detection from the reactive shift of a whispering-gallery mode” ©2008 by The National Academy of Sciences of the USA [14].

transcription qPCR (qRT-PCR) that integrates a rapid-cycle fiber optic PCR chamber with feedback-controlled laser heating and online fluorometric detection of PCR products [22–24] (Refer to Appendix A for definition of PCR, qPCR, RT-PCR). Central to this platform is a suitably tailored optical fiber, whose hollow core provides accommodation for all the PCR components and all the steps of the PCR cycles [25, 26]. Infrared laser radiation is used to provide rapid heating of the fiber optic PCR chamber up to the DNA melting point. The process of laser-induced heating is monitored in real-time by means of all-optical thermometry based on color centers of diamond nanoparticles, after the annealing and extension steps have been performed at lower temperatures as required, the PCR cycles are repeated, providing an exponential amplification of targeted DNA sequences. This process is monitored in real-time using DNA-bound fluorescent reporters driven by visible laser radiation, which is coupled to the hollow fiber core. With careful optimization of laser-induced heating and heat-removal geometry, the photonic version of PCR can radically reduce the PCR cycle duration relative to standard PCR machines, enabling faster testing as a key strategy to mitigate spread of infectious disease.

Our photonic PCR will enable rapid (i.e., as fast as 10 PCR cycles, each cycle being 1 min as described in a study by Li et al. [25]) and highly specific early detection of SARS-CoV-2 soon after infection—in most cases, even before the onset of disease’s symptoms [27–31] (typically 10–15 days), providing much-needed lead time for early treatment and disease spread prevention. When designed specifically for SARS-CoV-2 detection, photonic PCR would be run in the qRT-PCR mode. In this mode, a small amount of SARS-CoV-2 RNA present in a biomaterial sample (such

as saliva) is first converted into complementary DNA (cDNA) using reverse transcriptase and deoxynucleoside triphosphates (dNTPs) [32]. The cDNA produced through this process is then used as a template for exponential amplification via PCR.

Our photonic platform (Figure 6) is designed to accommodate all of the steps necessary for qPCR/qRT-PCR—denaturation, annealing, and extension. At the denaturation step, the fiber optic thermal cyclers is heated, using IR laser radiation, up to 94–98 °C, leading to denaturation of DNA/cDNA by breaking the hydrogen bonds between its bases, thus producing two single-

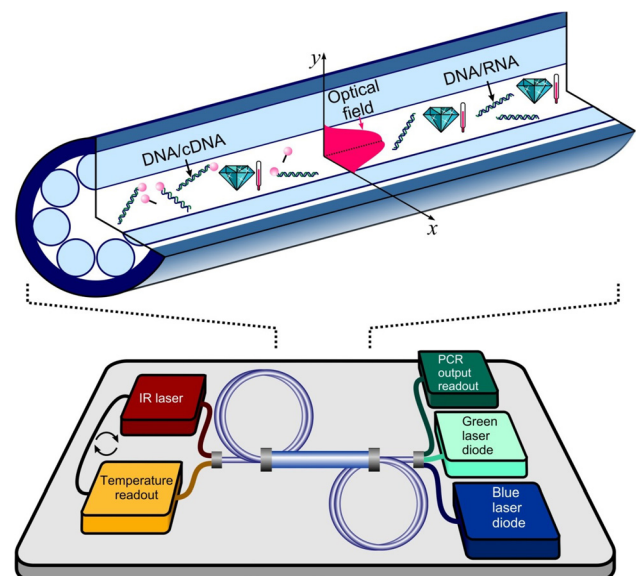


Figure 6: A photonic credit-card-size platform for rapid-cycle real-time polymerase chain reaction (qPCR) and reverse-transcription qPCR.

stranded DNA molecules. At the annealing step, the temperature is lowered to 50–65 °C, allowing left and right primers to base pair to their complementary sequences, thus bracketing the DNA region to be amplified. At the third step, the temperature of the fiber optic thermal cycler is maintained in a typical range of 72–80 °C, as the DNA polymerase synthesizes a new DNA strand complementary to the targeted DNA/cDNA strand by assembling free dNTPs from the reaction mixture to build new strands complementary to the template in the 5'-to-3' direction. Experimental and theoretical studies of photonic PCR suggest that a PCR master mix of volume Φ will require a nuclease-free water mixture of 0.005Φ of Taq DNA polymerase, 0.1Φ of $10\times$ standard Taq reaction buffer, 0.02Φ of 10 mM dNTPs, 0.02Φ of 10 μ M forward primer, and 0.02Φ of 10 μ M backward primer.

3 Bioconjugate techniques

This section addresses biological and biochemical terms for readers from other fields, as well as experimentalist who intend to implement these ideas as practical apparatus.

An essential component of the devices we discussed in Section 2 is the preparation of surfaces that are conjugated to bio molecules that we want to detect. Many techniques have been discussed in the literature and compiled in the classic book, *Bioconjugate Techniques* [33]. Since we are working with various optical fibers, it is natural for us to work with silane coupling agents, while other generic agents, e.g., protein A, G, A/G can be considered (see below).

Silanization is the process of adding silane groups (R3Si-) to a surface. The most useful compounds would be those containing a functional organic component, e.g., 3-glycid-oxy-propyl-trimethoxy-silane (GOPTS) and 3-glycidoxypropyltriethoxysilane that are very commonly used in fiber treatment. These compounds can be used to conjugate thiol-, amine-, or hydroxyl-containing ligands, depending on the pH of the reaction [33]. GOPTS is often used in bioconjugate applications, forming a polymer matrix linked by -Si-O-Si- bonds and binding to glass surfaces joining Si-O- bonds. Biomolecules, antibodies in particular in the context of this paper, can bond to fiber surfaces after reactions with the epoxy group in GOPTS.

Another method for attaching antihuman antibodies to the surface of an optical fiber optic is the use of proteins A, G, and L which are widely used in antibody purification procedures, where a specific antibody needs to be separated from the solution and purified. In some optical detection

devices [34, 35], proteins A and G are used to attach the antibody to a substrate that later can be used to detect specific viruses using optical techniques or the naked eye. Using polydopamine and protein G solution [35], any substrate can be functionalized such that the antibody can attach to the substrate using its Fc region. The protein-coated substrate (see Figure 7c), in our case, the hollow-core optical fiber, is primed to attach to the desired antihuman antibody using the Fc region (base, see Figure 7c). This strategy will allow will allow the Fab region of the antibody to be available to interact with the target human antibody (in this case, anti-SARS-CoV-2 IgG and IgM).

In addition, using a fluorescent molecule or, even better, an FNP conjugated to the spike protein of SARS-CoV-2, we can tag the specific antibodies against SARS-CoV-2. In this manner, we will be able to see the signal from very few FNPs or fluorescent molecules. We promote the use of FNPs because they do not bleach under excitation in contrast to fluorescent dyes. This will give us the opportunity to increase the acquisition time for the Charge-Coupled Device (CCD) camera and, as a result, the excitation time. Hence, we will be able to observe very low amounts of FNPs in a few minutes.

A variant of these methods could be coating the optical fiber with the spike protein from SARS-CoV-2. The sample will contain anti-SARS-CoV-2 IgGs and IgMs tagged with FNPs conjugated to antihuman antibodies. As the sample is introduced into the optical fiber, the anti-SARS-CoV-2 antibodies will attach to a substrate. Based on the same principle, we can see the signal from FNPs that are attached to the fiber through linkage between the spike protein and antispikes protein antibody tagged with FNPs conjugated with antihuman antibodies. Similar assays have been used to detect water pollutants [36].

Another method that can be used to attach antihuman antibodies to the substrate or optical fiber is to use sulfhydryl (-SH) groups that are naturally existing or added to the antihuman antibodies. In this method, the surface is activated by maleimide. Maleimide is a popular reagent for crosslinking sulfhydryl (-SH) groups, and it is used to form covalent links between the cysteine residues of proteins [37, 38]. Maleimide surfaces are obtained by aminosilanizing a surface with primary amines (-NH₂) and reacting them with the heterobifunctional crosslinker, Sulfo-SMCC [39]. The crosslinker sulfo-SMCC is added in order to activate the amino-modified surface. Finally, the sulfhydryl (-SH) groups on the antibody can attach to this substrate by covalent bonds.

The adaptability of our optic fiber approach to existing technologies will make the mass production of this system relatively straight forward and affordable. However,

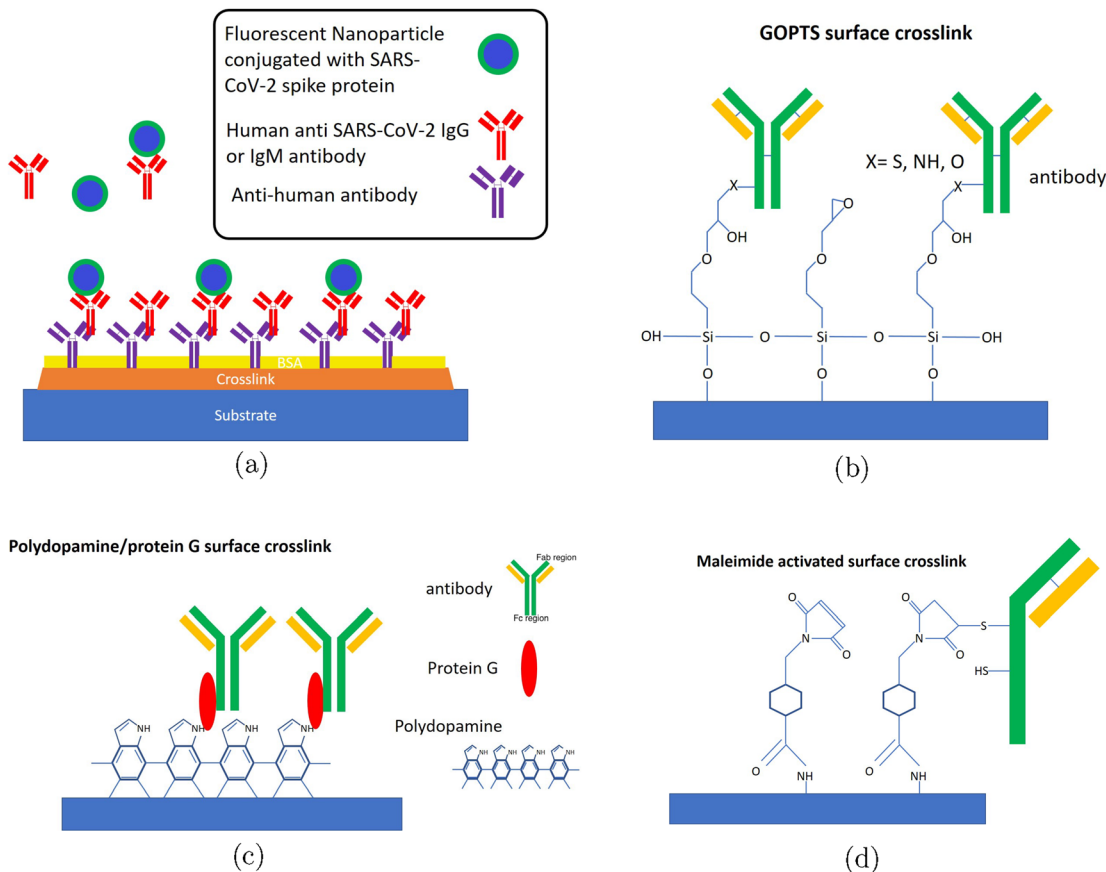


Figure 7: Schematic of substrate assay for detecting human anti-Severe Acute Respiratory Syndrome-Corona Virus-2 (SARS-CoV-2) IgG and IgM. The substrate is the inner surface of a hollow-core fiber optic. The cross-links we can use are 3-glycid-oxy-propyl-trimethoxy-silane (GOPTS), protein A or polydopamine/protein G, or amine-maleimide. The Bovine Serum Albumin (BSA) layer is used to block any other active part of the substrate. The human IgG and IgM bind to antihuman antibody by their Fc region, while the Fab region binds to spike proteins immobilized on the surface of a FNP.

depending on the type of test (PCR, antibody detection, etc.) one may need to choose the proper fiber optic setup and proper sample preparation. For instance, if original blood samples need to be tested, the hollow-core fiber optics chosen must have hollow regions large enough to accommodate for large blood cells. Perhaps, for certain detection applications such as antibodies or other proteins, one will need to filter and separate blood cells from the sample and only use blood plasma (or serum). This will reduce the interference caused by large objects such as red and white blood cells. This filtration can be integrated into the system like the sample pads in lateral flow assays (LFAs), which filter large particles and cells. Sample preparation can also be done before the test to promote the best result.

4 Discussion

One popular configuration for a COVID-19 test is the gold nanoparticle (AuNP) LFA configuration as shown in

Figure 8. In this type of setup, a drop of blood mixed with a buffer solution is placed on the sample pad and wicked by capillary action into the conjugation pad which contains gold nanoparticles coated with spiked protein from the SARS-CoV-2. In such a case, the spike protein-conjugated gold nanoparticle looks to an antibody like a virus and the antibody binds to the coated AuNP. This bound, conjugated, gold particle antibody, e.g., SARS-CoV-2-specific IgG, is then wicked downstream to a strip which contains anti-antibodies (i.e., secondary antibodies) which will now bind to the SARS-CoV-2 antibody-gold complex. When there are enough gold particles, the line looks red, and this signals the presence of COVID-19 disease. If there are no antibodies, the gold is swept downstream to the collection pad and a negative result (no infection) is recorded.

The COVID-19 “test setup” discussed in Section 2.1 has points in common with LFA and points which are quite different. For example, the fiber optic platform of Figure 2 replaces the wicking membrane of Figure 8. The gold NPs

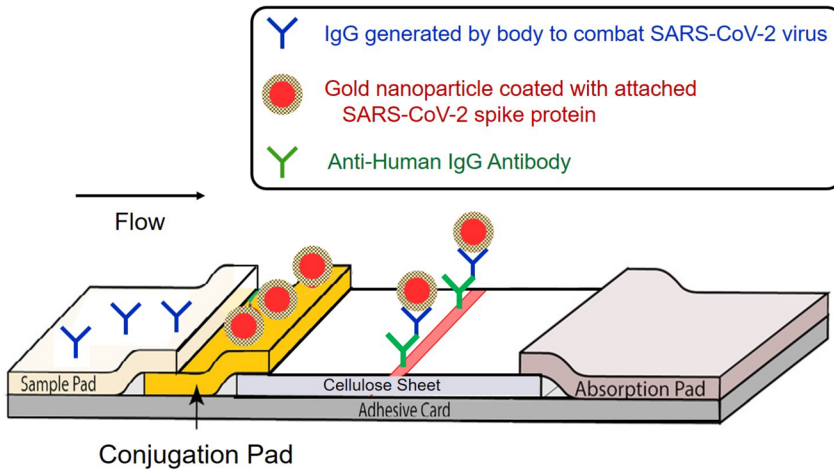


Figure 8: Schematic illustration for the wicking membrane with gold nanoparticle (NP) coated with Severe Acute Respiratory Syndrome-Corona Virus-2 (SARS-CoV-2) (see Table A1) spike protein. When the patient's blood with Corona Virus Disease-2019 (COVID-19) IgG (see Table A1) is flowed, assemblages of IgG and gold NP will be attached to the anti-antibody, and it can produce fluorescent light.

are replaced by the fluorescent NPs as in Figure 3. The fiber optical scheme is easily enclosed within a fiber optic cavity as in Figure 3a.

While antibody sensors provide a measure of the immune response to the virus, PCR is the technology of choice for early diagnostics, before any virus-specific antibodies can be detected in the bloodstream. Real-time state-of-the-art technique, qRT-PCR, which relies on optically excited fluorescent reporters, has become a gold standard in virus detection. The greatest downside of this well-established technology is the time it takes to run a test, limited by the PCR thermal cycle duration; it usually takes time to uniformly and precisely heat the sample volume and then cool it down and then heat again (1–5 days to complete traditional PCR and 45 min to complete qPCR [40]). The number of these cycles determines the DNA multiplication factor. With our fiber-based approach, we expect to have a significant scale-down of the reaction volume, and a corresponding reduction of characteristic cooling and heating time intervals. As a result, we expect to reduce the total time required to obtain test outcomes, to about 10 min. Within our approach, the heating and the temperature control will be conveniently provided through fiber-coupled laser-based methods. Naturally, our photonic qRT-PCR platform will incorporate an online fluorometric detection of PCR products. With careful optimization, this approach will lead to a greatly improved sensitivity, while reducing the test turnaround times, relative to standard PCR systems. In addition, the fiber optic approach, combined with microfluidics engineered for sample and reagent delivery, will allow compact design and scalability, resulting in affordable mass production and point-of-care implementation. Early detection of SARS-CoV-2 virions, enabled by the photonic fiber platform for qRT-PCR, will provide much-needed lead time for early treatment and prevention of disease spread.

Acknowledgments: M. O. S. thanks Chancellor John Sharp for many stimulating discussions and he thanks the Robert A. Welch Foundation, the Air Force Office of Scientific Research, the National Science Foundation (NSF), the Office of Naval Research, and King Abdulaziz City for Science and Technology (KACST) for support. The authors thank Jane Pryor, and Maria Bermudez Cruz for helpful discussions. N. R., S. D., C. L., S. E., M. L. are supported by the Herman F. Heep and Minnie Belle Heep Texas A&M University Endowed Fund held/administered by the Texas A&M Foundation. J. D. C. is supported in part from funds provided by the Texas A&M University System and National Institutes of Health Grant AI104960. P. H. acknowledges financial support from the Government of the Russian Federation (Mega-grant No. 14.W03.31.0028). G. S. A. thanks the Robert A. Welch Foundation grant no A-1943 and the AFOSR award No. FA9550-18-1-0141 for support. A. S. acknowledges the support from the Robert A. Welch Foundation grant no A-1547. A. Z. acknowledges support from the Welch Foundation (Grant No. A-1801-20180324). V. B. and A. Z. acknowledge support from the Russian Foundation for Basic Research (project Nos. 17-00-00212 and 17-00-00214). V. D. acknowledges support from German Research Foundation (CRC 1375 - NOA - C2). V.P. acknowledges the support of the U.S. Army Research Office under Grant W911NF-20-1-0204, the U.S. National Science Foundation under RAPID Grant IIS-2026982, and a grant from the C3.ai Digital Transformation Institute.

Author contribution: All the authors have accepted responsibility for the entire content of this submitted manuscript and approved submission.

Research funding: The research was supported by the Robert A. Welch Foundation (Grant No. A-1943, A-1547, and A-1261), the Air Force Office of Scientific Research (Award No. FA9550-20-1-0366 DEF), National Science Foundation (Grant No. PHY-2013771), Office of Naval

Research (Grant No. N00014-20-1-2184), Texas A&M Foundation, National Institutes of Health (Grant No. AI104960), and the Government of the Russian Federation (14.W03.31.0028). This research is also supported by King Abdulaziz City for Science and Technology (KACST).

Conflict of interest statement: The authors declare no conflicts of interest regarding this article.

Appendix A

Table A1: Summary of abbreviations.

CARS	Coherent anti-Stokes Raman scattering, a technique for using multiple photons for measuring molecular vibration with much greater sensitivity than ordinary (spontaneous) Raman emissions
COVID-19	The corona virus disease that appeared in late 2019
dNTP	Dinucleoside triphosphate, a precursor molecule for DNA
GOPTS	(3-Glycidyoxypropyl)trimethoxysilane is used as a coupling agent for many molecules with glass or mineral surfaces
IgG	The most abundant immunoglobulin (antibody) in human blood; SARS-CoV-2-specific IgG is made by B-cells of the immune system following detection of SARS-CoV-2; attaches to the virus spike protein
IgM	The first immunoglobulin (antibody) to form following detection of an antigen by the human immune system; short-lived relative to IgG
LF4 TAMRA (Figure 2f)	A fluorescent oligonucleotide primer molecule in the DNA polymerase system
NV diamond	Nanosize diamond crystals containing defects in the form of a vacant space next to a nitrogen atom; Such structures fluoresce upon impact of a laser beam of specified wavelength.
PCR/qPCR	Polymerase chain reaction, the process of making new copies of an original sample of DNA (q indicates the quantitative version of PCR)
RT-PCR/qRT-PCR	Quantitative reverse transcriptase PCR, the process of using the enzyme, reverse transcriptase, to read a molecule of RNA (or a fragment, thereof) to form the complementary DNA
SARS-CoV-2	Severe Acute Respiratory Syndrome-Corona Virus-2, The causative viral agent of COVID-19
Taq DNA polymerase	A thermal-stable DNA polymerase (enzyme)
Sulfo-SMCC	A protein containing an amine-sulfo-NSH-ester on one end and melamide on the other. The former increases water solubility; the latter reacts with SH groups.

Appendix B Whispering gallery modes

Let us consider a dielectric cylinder with a refractive index n and radius R . Maxwell's equation for the dielectric medium with inhomogeneous refractive index $n(\mathbf{r})$ reads

$$\nabla^2 \mathbf{E} - \nabla (\operatorname{div} \mathbf{E}) - \frac{1}{c^2} \frac{\partial^2}{\partial t^2} (n^2(\mathbf{r}) \mathbf{E}) = 0. \quad (9)$$

We look for normal modes of the field in the form

$$\mathbf{E}(\mathbf{r}) = E(r) e^{-i\omega t + im\phi} \hat{z}, \quad (10)$$

where r , ϕ , and z are cylindrical coordinates, \hat{z} is a unit vector along the cylinder's axis z , and m is the angular quantum number. The mode function (10) is transverse, that is $\operatorname{div}(\mathbf{E}) = 0$. In addition, the mode function (10) is independent of z , that is electromagnetic wave does not propagate along the axis of the cylinder.

The Maxwell's Eq. (9) yields that radial part of the mode function (10) inside the cylinder ($r < R$) is given by the cylindrical Bessel function

$$E(r) = C_1 J_m\left(\frac{\omega n}{c} r\right), \quad (11)$$

and by the Hankel function of the first kind outside the cylinder ($r > R$)

$$E(r) = C_2 H_m^{(1)}\left(\frac{\omega}{c} r\right). \quad (12)$$

Solution outside the cylinder describes an outgoing cylindrical wave, and at $r \gg R$ the asymptotic of the electric field is

$$E(t, \mathbf{r}) \sim \frac{1}{\sqrt{r}} e^{i\omega\left(\frac{r}{c} - t\right) + im\phi}.$$

The outgoing cylindrical wave carries energy out of the system and the modes decay with time. The decay rate Γ is given by the imaginary part of the mode frequency

$$\Gamma = -\operatorname{Im}(\omega).$$

The normal mode frequencies can be found by imposing the boundary conditions at the cylinder surface, namely, $E(r)$ and $\partial E(r)/\partial r$ must be continuous at $r = R$. This gives a transcendental characteristic equation for ω

$$n \frac{J_m'\left(\frac{\omega n}{c} R\right)}{J_m\left(\frac{\omega n}{c} R\right)} = \frac{H_m^{(1)'}\left(\frac{\omega}{c} R\right)}{H_m^{(1)}\left(\frac{\omega}{c} R\right)}, \quad (13)$$

where the prime denotes differentiation with respect to the argument of the Bessel function.

For fixed m , Eq. (13) has an infinite number of solutions which are labeled by the radial quantum

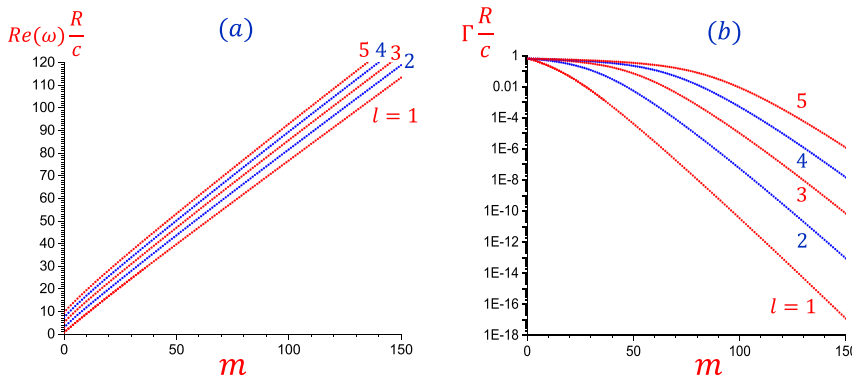


Figure 9: Normal mode frequencies (a) and their decay rates Γ (b) as a function of the angular quantum number m for the radial quantum number $l = 1, 2, 3, 4,$ and 5 , obtained by numerical solution of Eq. (13) with $n = 1.4$.

number $l = 1, 2, 3, \dots$. The radial quantum number l determines the number of field oscillations inside the cylinder. In Figure 9, we plot the normal mode frequencies (a) and their decay rates (b) as functions of the angular quantum number m for $l = 1, 2, 3, 4,$ and 5 . In these calculations, we assume that cylinder's refractive index is $n = 1.4$. The vertical axis in Figure 9b has a logarithmic scale.

Figure 9b shows that the decay rate of the modes with large m is exponentially small. The decay rate of the mode is smallest for $l = 1$. The modes with $l = 1$ and large m are known as the WGMs. They are a wave analog to a ray reflecting m times off the edge of the cavity at a grazing angle by total internal reflection forming a standing wave.

For large m , the quality factor, Q , of the dielectric microresonators could be only limited by the intrinsic material absorption. A typical value of Q for such microresonators is of the order of 10^8 .

High Q implies a narrow resonance width $\Delta\omega = \omega/Q$ or $\Delta\lambda = \lambda/Q$. For example, if the resonance wavelength is $\lambda = 1 \mu\text{m}$ then the width of the resonance is about 10 fm . Such small value of the resonance width allows us to measure the resonance frequency shift produced by a single virus molecule attached to the surface of the microresonator. As molecules bind to the surface, the resonant wavelength position, λ , jumps, creating steps in the time dependence $\lambda(t)$. Such steps have been observed, e.g., in the experiment of Armani et al. with interleukin-2 molecules [41].

References

- [1] J. S. Ellis and M. C. Zambon, "Molecular diagnosis of influenza," *Rev. Med. Virol.*, vol. 12, pp. 375–389, 2002.
- [2] M. O. Scully, G. W. Kattawar, R. P. Lucht, et al., "FAST CARS: engineering a laser spectroscopic technique for rapid identification of bacterial spores," *Proc. Natl. Acad. Sci. U. S. A.*, vol. 99, no. 17, pp. 10994–11001, 2002.
- [3] S. O. Konorov, A. M. Zheltikov, and M. Scalora, "Photonic-crystal fiber as a multifunctional optical sensor and sample collector," *Opt. Express*, vol. 13, pp. 3454–3459, 2005.
- [4] I. A. Bufetov, A. F. Kosolapov, A. D. Pryamikov, et al., "Revolver hollow core optical fibers," *Fibers*, vol. 6, p. 39, 2018.
- [5] P. St and J. Russell, "Photonic crystal fibers," *Science*, vol. 299, pp. 358–362, 2003.
- [6] A. M. Zheltikov, "Holey fibers," *Phys. Usp.*, vol. 43, pp. 1125–1136, 2000.
- [7] A. B. Fedotov, S. O. Konorov, V. P. Mitrokhin, E. E. Serebryannikov, and A. M. Zheltikov, "Coherent anti-Stokes Raman scattering in isolated air-guided modes of a hollow-core photonic-crystal fiber," *Phys. Rev. A*, vol. 70, p. 045802, 2004.
- [8] A. M. Zheltikov, "Nonlinear optics of microstructure fibers," *Phys. Usp.*, vol. 47, pp. 69–98, 2004.
- [9] M. Scully and S. Zubairy, *Quantum Optics*, Cambridge, Cambridge University Press, 1996, <https://doi.org/10.1017/CBO9780511813993>.
- [10] G. S. Agarwal, *Quantum Optics*, Cambridge, Cambridge University Press, 2013, p. 175, <https://doi.org/10.1017/CBO9781139035170>.
- [11] K. J. Vahala, "Optical microcavities," *Nature*, vol. 424, pp. 839–846, 2003.
- [12] M. L. Gorodetsky, A. A. Savchenkov, and V. S. Ilchenko, "Ultimate Q of optical microsphere resonators," *Opt. Lett.*, vol. 21, pp. 453–455, 1996.
- [13] A. A. Savchenkov, A. B. Matsko, V. S. Ilchenko, and L. Maleki, "Optical resonators with ten million finesse," *Opt. Express*, vol. 15, pp. 6768–6773, 2007.
- [14] F. Vollmer, S. Arnold, and D. Keng, "Single virus detection from the reactive shift of a whispering-gallery mode," *Proc. Natl. Acad. Sci. U. S. A.*, vol. 105, no. 52, pp. 20701–20704, 30 Dec. 2008.
- [15] J. Zhu, S. K. Ozdemir, Y. Xiao, et al., "On-chip single nanoparticle detection and sizing by mode-splitting in an ultra-high-Q microresonator," *Nat. Photonics*, vol. 4, p. 46, 2010.
- [16] F. Giovanardi, A. Cucinotta, A. Rozzi, et al., "Hollow core inhibited coupling fibers for biological optical sensing," *J. Lightwave Technol.*, vol. 37, no. 11, 1 Jun. 2019, <https://doi.org/10.1109/JLT.2019.2892077>.
- [17] V. Ahsani, F. Ahmed, M. B. G. Jun, and C. Bradley, "Tapered fiber-optic Mach-Zehnder interferometer for ultra-high sensitivity measurement of refractive index," *Sensors*, vol. 19, p. 1652, 2019.

- [18] Y. Liu, P. Hering, and M. O. Scully, "An integrated optical sensor for measuring glucose concentration," *Appl. Phys.*, vol. B54, pp. 18–23, 1992.
- [19] J. L. Dominguez-Juarez, G. Kozyreff, J. Martorell, "Whispering gallery microresonators for second harmonic light generation from a low number of small molecules", *Nat. Commun.*, vol. 2, 2011, Art no. 254. <https://doi.org/10.1038/ncomms1253>.
- [20] R. Gao, D. Lu, M. Zhang, and Z. Qi, "Optofluidic immunosensor based on resonant wavelength shift of a hollow core fiber for ultratrace detection of carcinogenic benzo[a]pyrene," *ACS Photonics*, vol. 5, pp. 1273–1280, 2018.
- [21] S. Dutta Gupta and G. S. Agarwal, "Strong coupling cavity physics in microspheres with whispering gallery modes," *Opt. Commun.*, vol. 115, p. 597, 1995.
- [22] I. V. Fedotov, S. Blakley, E. E. Serebryannikov, et al., "Fiber-based thermometry using optically detected magnetic resonance," *Appl. Phys. Lett.*, vol. 105, p. 261109, 2014.
- [23] I. V. Fedotov, L. V. Doronina-Amitonova, D. A. Sidorov-Biryukov, et al., "Fiber-optic magnetic-field imaging," *Opt. Lett.*, vol. 39, pp. 6954–6957, 2014.
- [24] S. Blakley, X. Liu, I. Fedotov, et al., "Fiber-optic quantum thermometry with germanium-vacancy centers in diamond," *ACS Photonics*, vol. 6, pp. 1690–1693, 2019.
- [25] X. Li, L. V. Nguyen, K. Hill, et al., "Picoliter real-time quantitative polymerase chain reaction (qPCR) in an all-fiber system," in *Asia Communications and Photonics Conference (ACPC) 2019, OSA Technical Digest*, Optical Society of America, 2019. paper S4G.5.
- [26] J. M. Mauro, L. K. Cao, L. M. Kondracki, S. E. Walz, and J. R. Campbell, "Fiber-optic fluorometric sensing of polymerase chain reaction-amplified DNA using an immobilized DNA capture protein," *Anal. Biochem.*, vol. 235, pp. 61–72, 1996.
- [27] M. M. Arons, K. M. Hatfield, S. C. Reddy, et al., "Presymptomatic SARS-CoV-2 infections and transmission in a skilled nursing facility," *N. Engl. J. Med.*, 2020, <https://doi.org/10.1056/NEJMoa2008457>, Epub ahead of print.
- [28] S. Hoehl, H. Rabenau, A. Berger, et al., "Evidence of SARS-CoV-2 infection in returning travelers from Wuhan, China," *N. Eng. J. Med.*, vol. 283, pp. 1278–1280, 2020.
- [29] K. Q. Kam, C. F. Yung, L. Cui, et al., "A well infant with coronavirus disease 2019 with high viral load," *Clin. Infect. Dis.*, 2020, <https://doi.org/10.1093/cid/ciaa201>.
- [30] T. Q. M. Le, T. Takemura, M. L. Moi, et al., "Severe acute respiratory syndrome coronavirus 2 shedding by travelers, Vietnam, 2020," *Emerg. Infect. Dis.*, p. 26, 2020, <https://doi.org/10.3201/eid2607.200591>.
- [31] L. Zou, F. Ruan, M. Huang, et al., "SARS-CoV-2 viral load in upper respiratory specimens of infected patients," *N. Engl. J. Med.*, vol. 382, pp. 1177–1179, 2020.
- [32] E. A. Bruce, S. Tighe, J. J. Hoffman, et al., "RT-qPCR detection of Sars-Cov-2 RNA from patient nasopharyngeal swab using Qiagen Rneasy kits or directly via omission of an RNA extraction step", 2020, bioRxiv 2020.03.20.001008, <https://doi.org/10.1101/2020.03.20.001008>.
- [33] G. T. Hermanson, *Bioconjugate Techniques*, London, Academic Press, 2013, <https://doi.org/10.1016/C2009-0-64240-9>.
- [34] A. A. Yanik, M. Huang, O. Kamohara, et al., "An optofluidic nanoplasmonic biosensor for direct detection of live viruses from biological media," *Nano Lett.*, vol. 10, no. 12, pp. 4962–4969, 2010.
- [35] J. Moon, J. Byun, H. Kim, et al., "Surface-independent and oriented immobilization of antibody via one-step polydopamine/protein G coating: application to influenza virus immunoassay," *Macromol. Biosci.*, vol. 19, p. 1800486, 2019.
- [36] A. Hlaváček, Z. Farka, M. Hübner, et al., "Competitive upconversion-linked immunosorbent assay for the sensitive detection of diclofenac," *Anal. Chem.*, vol. 88, no. 11, pp. 6011–6017, 2016.
- [37] <http://tools.thermofisher.com/content/sfs/brochures/TR0005-Attach-Ab-glass.pdf>.
- [38] D. Kim and A. E. Herr, "Protein immobilization techniques for microfluidic assays," *Biomicrofluidics*, vol. 7, no. 4, p. 041501, Jul. 2013.
- [39] A. Sen, "Quantification of cell attachment on different materials as candidate electrodes for measurement of quantal exocytosis," PhD thesis, <https://doi.org/10.32469/10355/5722>.
- [40] M. J. Espy, J. R. Uhl, L. M. Sloan, et al., "Real-time PCR in clinical microbiology: application for routine laboratory testing," *Clin. Microbiol. Rev.*, vol. 19, no. 1, pp. 165–256, Jan. 2006.
- [41] A. M. Armani, R. P. Kulkarni, S. E. Fraser, R. C. Flagan, and K. J. Vahala, "Label-free, single-molecule detection with optical microcavities," *Science*, vol. 317, p. 783, 2007.